Polar feedbacks in radiative-advective equilibrium from an air mass transformation perspective

Rodrigo Caballero[a] and Timothy M. Merlis[b]

[a] *Department of Meteorology and Bolin Centre for Climate Research, Stockholm University, Stockholm, Sweden*

[b] *Program in Atmospheric and Oceanic Sciences, Princeton University, Princeton, New Jersey*

This is a non peer-reviewed pre-print submitted to EarthArXiv, and is currently in review at Journal of Climate.

Corresponding author: Rodrigo Caballero, rodrigo.caballero@misu.su.se

ABSTRACT: We develop a novel single-column model of clear-sky radiative-advective equilibrium where advective heating is internally determined by relaxing the column temperature and humidity toward fixed midlatitude profiles, consistent with an air-mass transformation perspective. The model reproduces observed polar temperature and advective heating rate profiles, and also captures many of the climate-change responses found in climate models. Exploring the model's physics, we show that the surface-based temperature inversion develops by ceding energy downwards to the surface, which then radiates this energy to space; we name this the "surface radiator fin" effect. We use the model to address three outstanding questions regarding polar climate change: (i) What mechanisms control polar lapse-rate change? (ii) What determines the known compensation between changes in dry and moist energy transport? and (iii) What is the most physically consistent way to decompose forcing and feedbacks at the poles? In answer to these questions, we show that: (i) Three mechanisms control the lapse-rate response to warming: weakening of the surface radiator fin, increased radiative cooling by free-tropospheric water vapor emission, and relaxation toward the external profile anomaly; all three increase the lapse rate as climate warms. (ii) Compensation between dry and moist advective heating results from a delicate balance between changes in the boundary layer and the free troposphere, with no constraints imposing precise compensation. (iii) Remote advective influence on the poles should be considered a forcing, while lapse-rate and advective heating changes should not be treated as separate feedbacks but rather as part of the temperature feedback.

1. Introduction

The concept of radiative-convective equilibrium (RCE) and its embodiment in a single-column model (Manabe and Strickler 1964; Manabe and Wetherald 1967) is the foundation of our understanding and quantification of climate sensitivity (see review by Jeevanjee et al. 2022). RCE prevails when the atmosphere is heated from below and atmospheric radiative cooling to space is balanced by upward turbulent fluxes at the surface. In RCE, surface and atmospheric temperature are strongly coupled while atmospheric temperature is constrained to follow a moist adiabatic profile, imposing a tight connection between surface temperature and top-of-atmosphere (TOA) energy fluxes. As a result, a unit perturbation of TOA flux will give the same surface temperature response regardless of which forcing or feedback agent provides the perturbation. This fungibility motivates the now-conventional TOA forcing-feedback decomposition (Manabe and Wetherald 1980; Sherwood et al. 2015). This decomposition includes a separate lapse-rate feedback, which is reasonable since in RCE the lapse-rate feedback is constrained by the moist adiabat and constitutes a distinct physical mechanism.

The opposite limit to RCE is radiative-advective equilibrium (RAE), where convection is absent, surface turbulent fluxes are small or downwards, and diabatic cooling is primarily balanced by lateral energy flux convergence (Payne et al. 2015; Cronin and Jansen 2016). RAE prevails in the polar regions, especially in winter (Miyawaki et al. 2022, 2023). RAE is therefore crucial to polar amplification—the enhanced warming of the poles in response to global forcing that is a robust but still not fully understood feature of Earth's climate sensitivity (Previdi et al. 2021; Taylor et al. 2022). This motivates interest in developing a minimal model of RAE that robustly captures the basic physics of high-latitude climate, as a counterpart to single-column RCE for lower latitudes.

Substantial progress has been made in this direction (Payne et al. 2015; Cronin and Jansen 2016; Henry and Merlis 2020; Henry et al. 2021; Freese and Cronin 2021). This previous work shows that RAE is profoundly different from RCE. In RAE, fungibility is lost: the surface response to unit TOA forcing depends on the nature of the forcing. Also, different forcings affect the lapse rate differently; for example, changes in greenhouse gases and in surface solar absorption both give a bottom-amplified response, while changes in advective heating tend to stabilize the atmosphere. This means that it no longer makes sense to think of lapse-rate feedback as a single, standalone mechanism but rather as the residual of disparate effects. It also raises basic questions, such as why a well-mixed gas like CO_2 should give a similar lapse-rate response to a surface forcing, and why both of these are different from the response to advective heating. These are important questions considering the major role attributed to lapse-rate feedback in explaining polar amplification by the conventional TOA decomposition (Pithan and Mauritsen 2014; Hahn et al. 2021).

The central difficulty in formulating a single-column RAE model is how to specify advective heating. Advection depends on horizontal gradients and is intrinsically non-local, contrary to the locality of a single-column model. In the prior work cited above, this problem is circumvented by simply prescribing a fixed profile of advective heating. But in RAE, advective heating must balance diabatic cooling. A change to radiative cooling within the column—due for example to changing greenhouse gas concentrations—will automatically result in changed advective heating. Keeping advective heating fixed breaks this physical connection between polar energy convergence and other forcings and feedbacks (Feldl et al. 2017; Russotto and Biasutti 2020; Beer and Eisenman 2022). Advective heating should be internally determined as part of the solution, but this requires information about extra-polar fields not available in a single polar column.

A potential way out of this impasse is suggested by the results of climate model simulations where radiative forcing is applied within limited latitude bands (Chung and Räisänen 2011; Yoshimori et al. 2017; Shaw and Tan 2018; Stuecker et al. 2018; Semmler et al. 2020). These simulations all show that while the poles respond strongly to forcing applied in lower latitudes, the opposite is not true: midlatitude temperatures are to a first approximation unaffected by polar forcing. This suggests that conditions at the poleward edge of the midlatitudes provide a boundary condition for the polar climate. By appropriately applying this boundary condition to a single-column model, it would possible to simulate changes internal to the polar column while keeping this boundary condition fixed, or simulate remote effects on the poles by changing the boundary condition, all while allowing advective heating to adjust in a physically consistent way.

Here, our first aim is to search for a simple yet sufficiently realistic way to apply the boundary condition. In Section 2, we show that advective heating can be approximated as a simple relaxation toward specified temperature and humidity profiles representative of midlatitude conditions, and provide empirical justification for this approximation. We implement it in a single-column model using realistic radiation, a simple turbulence scheme and assuming clear-sky conditions. Testing this model against reanalysis shows satisfactory results.

Our second aim is to explore the single-column model to better understand the nature of the RAE regime and its response to local and remote perturbations (Sections 3–7). We address the following specific questions:

1. What mechanisms control the polar lapse-rate response to global warming? More fundamentally, why is there a climatological surface-based temperature inversion in the first place, and what controls its strength?

2. Why do changes in moist and dry energy transport to the poles tend to compensate each other (Hwang et al. 2011)—are there any strong constraints acting to enforce this compensation?

3. What is the best way to decompose forcing and feedbacks at the poles?

The relaxation approach used in the single-column model developed here connects directly with the air-mass transformation perspective on polar climate (Pithan et al. 2018). In this perspective, midlatitude maritime air masses are advected into the polar cap, cool diabatically, and exit as polar air masses with lower temperature and humidity. The polar cap is continuously ventilated by an ensemble of such transient air-mass transformation events, and the steady-state single column model aims to capture the average effect of an ensemble of such events. We will emphasize this perspective throughout the paper, as it proves useful in gaining intuitive understanding of the model's behavior.

2. The single-column model

a. A simple expression for polar advective heating

We begin by writing the temperature tendency $\partial_t T$ at a given point in the polar atmosphere as

$$\partial_t T = Q_{\mathrm{rad}} + Q_{\mathrm{dif}} + Q_{\mathrm{dry}} + Q_{\mathrm{lat}} \tag{1}$$

where Q_{rad} is the radiative cooling rate, Q_{dif} is the heating or cooling rate due to diffusive energy fluxes by small-scale turbulence, Q_{dry} is the advective heating rate due to dry static energy convergence by the large-scale flow, and Q_{lat} is the heating rate due to net condensation and latent heat release. This expression assumes that the polar atmosphere is always statically stable and there is no convective heating term.

In steady state, or for long-term averages, the net condensation rate equals the rate of moisture convergence. In this case, the last two terms on the r.h.s. can be written in terms of the moist static energy (MSE) convergence:

$$Q_{\mathrm{adv}} \equiv Q_{\mathrm{dry}} + Q_{\mathrm{lat}} = -\frac{1}{c_p}\nabla\cdot(\mathbf{u}h) \tag{2}$$

where $\mathbf{u} = (u, v, \omega)$ is the three-dimensional large-scale wind and $h = c_p T + \ell_v q + gz$ is the MSE, with c_p the specific heat of air, ℓ_v the latent heat of condensation, q the specific humidity and gz the geopotential, and we have defined Q_{adv} as the total advective heating rate. Averaging (2) horizontally over a polar cap (i.e. the region poleward of a given latitude line) and using the divergence theorem yields

$$c_p \overline{Q}_{\mathrm{adv}} = \frac{1}{L}[vh] - \partial_p \overline{\omega h} \tag{3}$$

where $\overline{(\cdot)}$ indicates an area average over the cap, $[\cdot]$ indicates a zonal average around the edge of the cap, and $L = C/A$ with C the circumference and A the area of the cap. Separating mean and eddy components, (3) can be rewritten as

$$c_p \overline{Q}_{\mathrm{adv}} = \underbrace{\frac{1}{L}[v]\left([h]-\overline{h}\right) - \overline{\omega}\,\partial_p \overline{h}}_{\text{MMC}} + \underbrace{\frac{1}{L}[v^* h^*]}_{\substack{\text{Horizontal}\\ \text{eddy}}} - \underbrace{\partial_p \overline{\omega' h'}}_{\substack{\text{Vertical}\\ \text{eddy}}} \tag{4}$$

where stars and primes indicate deviations from the zonal and polar-cap mean respectively. The first two terms on the r.h.s. represent MSE convergence by the mean meridional circulation (MMC), the third term represents horizontal MSE convergence by eddies around the edge of the polar cap, and the last term represents vertical MSE redistribution by eddies within the polar cap.

The horizontal eddy term can further be rewritten in terms of inward- and outward-oriented fluxes defined as

$$v^{\mathrm{in}} = [H(v^*)\,v^*], \quad h^{\mathrm{in}} = \frac{1}{v^{\mathrm{in}}}[H(v^*)\,v^* h], \quad h^{\mathrm{out}} = \frac{1}{-v^{\mathrm{in}}}[H(-v^*)\,v^* h], \tag{5}$$

where H is the Heaviside function and we have used $[v^* h^*] = [v^* h]$. In the Northern Hemisphere, v^{in} is the eddy mass flux flowing *into* the polar cap, while h^{in} and h^{out} are the mass-flux-weighted mean MSE values of air flowing into and out of the cap respectively. With these definitions, the horizontal eddy term becomes

$$\frac{1}{L}[v^* h^*] \;=\; -\frac{1}{\tau}\left(h^{\text{out}} - h^{\text{in}}\right) \tag{6}$$

where

$$\frac{1}{\tau} = \frac{v^{\text{in}}}{L}.$$

To understand the relative importance of the various terms in (4), we evaluate them directly using the ERA-Interim reanalysis product. We use 6-hourly data on pressure levels, masking out 'underground' regions where pressure is greater than surface pressure. Following previous work (Overland and Turet 1994; Cardinale et al. 2021), the vertical mean is removed from $[v]$ to exclude spurious contributions from net mass convergence. Results at 65°N (Figure 1c) show that the MMC term in (4) is much smaller than the horizontal eddy term at all levels. Similar results are obtained for other latitudes of the equatorward edge of the polar cap between 60-80°N (not shown). The negligible role played by the MMC in the Arctic is very different from the situation in the tropics, where weak temperature gradient constraints mean that radiative cooling is mostly balanced by $\overline{\omega}\partial_p\overline{h}$ (Sobel and Bretherton 2000).

Separating the horizontal eddy term into its three MSE components (Figure 1d) shows that the geopotential convergence term is also negligible, which is not surprising since pressure levels are close to horizontal at a given latitude. Attempts to compute the vertical eddy term fail however, yielding unrealistically large values likely due to problems with local mass balance arising from the interpolation to pressure coordinates and from errors in the analysis itself which produce unphysical large-amplitude noise in the ω' field (Trenberth 1991).

Given these results, we make the following approximations: (i) neglect the MMC term; (ii) neglect the geopotential component of the MSE convergence; (iii) neglect the vertical eddy term. Approximation (iii) cannot be directly justified from our observational analysis, but will be validated a posteriori as discussed below. With these approximations, our final expression for the polar-mean advective heating rate becomes simply

$$\overline{Q}_{\text{adv}} \;\approx\; -\frac{1}{\tau}\left(T_e^{\text{out}} - T_e^{\text{in}}\right) \tag{7}$$

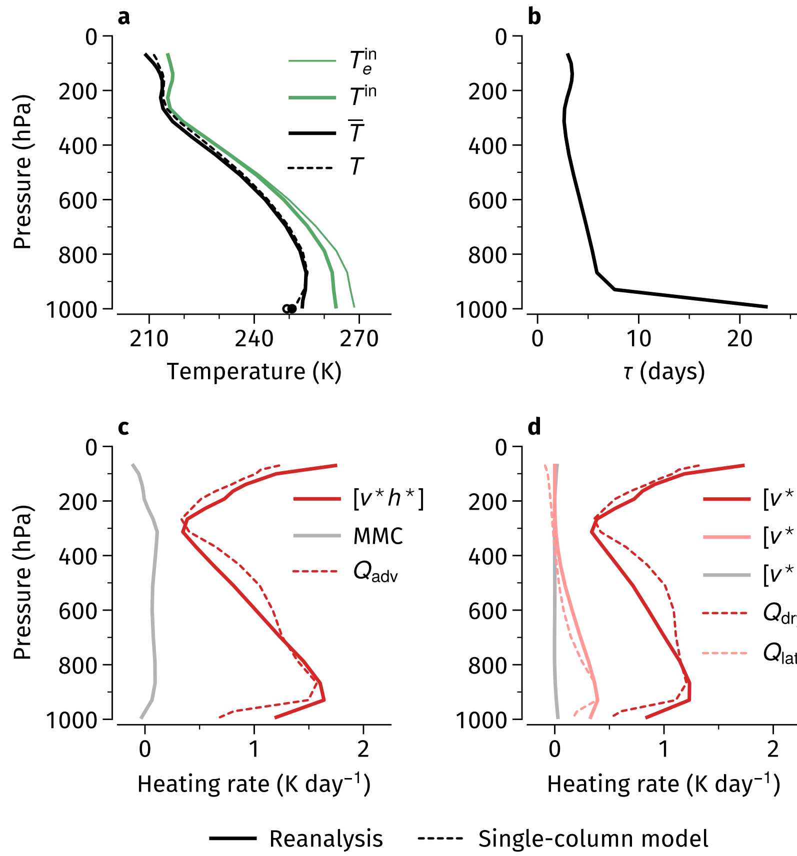

FIG. 1. (a) Temperatures, (b) ventilation timescale and (c,d) advective heating rates for the polar cap bounded by 65°N latitude. In all panels, solid lines show climatologies computed from the ERA-Interim reanalysis for winter (December-February) of 1980-2018, dotted lines show steady-state results for a single-column model simulation using the reanalysis T_e^{in} and τ profiles in (a,b) as input. In (a), dots along the bottom show surface temperature in reanalysis (filled) and model (hollow).

where

$$T_e = T + \frac{\ell_v}{c_p} q \tag{8}$$

is approximately the equivalent temperature at fixed pressure.

Expression (7) can be interpreted in two ways. From an Eulerian perspective, it can be seen as a coarse-grained advection, with a wind v^{in} acting on a gradient $(T_e^{\text{out}} - T_e^{\text{in}})/L$. From a Lagrangian air-mass transformation perspective, τ is a ventilation timescale, the typical time taken for an air parcel to cross the polar cap—note that L is roughly the diameter of the cap, and Figure 1b shows

$\tau \sim 5$ days at 800-900 hPa, consistent with the crossing timescale found in Lagrangian studies (Woods and Caballero 2016). Air parcels enter the polar cap with equivalent temperature T_e^{in}, travel isobarically while cooling radiatively and diffusively for a time τ, and exit with the smaller equivalent temperature T_e^{out}; the rate of energy convergence is proportional to the resulting energy drop. Both perspectives are equally valid, but we will emphasize the air-mass transformation perspective here since it makes explicit the tight connection between lateral energy convergence and diabatic cooling within the polar column.

b. Model implementation

We specify the single-column model as

$$\partial_t T \;=\; \underbrace{Q_{\text{rad}} \;+\; Q_{\text{dif}}}_{Q_{\text{dia}}} \;+\; \underbrace{Q_{\text{dry}} \;+\; Q_{\text{lat}}}_{Q_{\text{adv}}} \tag{9}$$

where T is a prognostic temperature profile controlled by the diabatic cooling rate $Q_{\text{dia}} = Q_{\text{adv}} + Q_{\text{dif}}$ and the advective heating rate $Q_{\text{adv}} = Q_{\text{dry}} + Q_{\text{lat}}$. Using (7) and taking the outflow temperature T^{out} as the column temperature T, we obtain

$$Q_{\text{dry}} \;=\; -\frac{1}{\tau}\left(T - T^{\text{in}}\right), \qquad Q_{\text{lat}} \;=\; -\frac{1}{\tau}\frac{\ell_v}{c_p}\left(\text{RH}\, q_{\text{sat}}(T) - q^{\text{in}}\right) \tag{10}$$

where T^{in} and q^{in} are prescribed inflow temperature and specific humidity, q_{sat} is saturation specific humidity and RH is a prescribed relative humidity.

Equation (10) realises the goal of expressing remote effects on the polar column as a relaxation to prescribed external temperature and humidity profiles, an approach originally suggested (though not developed) by Cronin and Jansen (2016). Note that since the column temperature is generally much colder than the inflow temperature, $q_{\text{sat}}(T) \ll q^{\text{in}}$ and the total advective heating rate can be approximated as $Q_{\text{adv}} \approx \tau^{-1}(T - T_e^{\text{in}})$, i.e. as a relaxation of the column temperature toward the inflow equivalent temperature T_e^{in}. However, we retain the full form of (10) in the model.

At its lower boundary, the column is coupled to a surface slab of fixed heat capacity c and temperature T_s:

$$c\,\partial_t T_s \;=\; F_{\text{rad}} \;+\; F_{\text{SH}} \;+\; F_s \tag{11}$$

where F_{rad} is the net surface longwave radiative flux and F_{SH} is the surface sensible heat flux, computed using the bulk-aerodynamic formulation $F_{\mathrm{SH}} = \gamma(T_0 - T_s)$ where T_0 is atmospheric temperature at the lowest model level and γ is a fixed exchange coefficient. Surface latent heat flux is neglected. As in previous work (Payne et al. 2015; Henry et al. 2021), we include a prescribed surface energy source F_s to represent absorbed surface insolation, ocean energy convergence into the slab, or the sum of both.

Radiative fluxes and cooling rate Q_{rad} are computed using the longwave radiative transfer scheme of the NCAR CAM3 model (Collins et al. 2004), with only water vapor and CO_2 as radiatively-active gases. We assume clear-sky conditions and neglect atmospheric solar absorption. Turbulent fluxes and heating rate Q_{dif} are computed using a simple diffusive scheme with fixed diffusivity applied to potential temperature, as described in Caballero et al. (2008). Humidity diffusion is neglected.

The complete model is implemented in practice using the CliMT framework (Monteiro and Caballero 2016; Monteiro et al. 2018, we use the "classic" version here). The column is discretized into 26 levels using the native CAM3 model grid (Collins et al. 2004), which is non-uniform in pressure with more tightly spaced levels near the surface, improving resolution in the boundary layer. The model is time-marched until the temperature profile reaches steady state, and all results shown below refer to this steady state. Note that all simulations presented here do in fact converge to a fixed point and show no oscillatory or chaotic behavior.

c. Design of simulations and forcing-feedback decomposition

To define a simulation, the following parameters need to be specified: inflow equivalent temperature T_e^{in}, ventilation rate $1/\tau$, CO_2 concentration, surface heat source F_s, relative humidity RH, kinematic diffusivity ν for the turbulence scheme, and surface exchange coefficient γ. All simulations in this paper use $\gamma = 6.55$ W m^{-2} K^{-1} and a vertically uniform RH = 80%. Diffusivity follows an exponentially-decaying profile $\nu = \nu_s \exp(-(p_s - p)/\Delta p)$ with a surface value $\nu_s = 1$ m^2 s^{-1} and a decay rate $\Delta p = 400$ hPa; this is done to avoid excessive diffusion around the tropopause. Other parameters vary as described below.

To explore the model's basic physics, we define a set of simulations using simplified settings: τ is vertically uniform, and T_e^{in} is specified by defining T^{in} as a profile with a constant lapse rate of

6 K km^{-1} from a surface temperature T_0^{in} up to an isothermal stratosphere at 210 K, and q^{in} as the corresponding specific humidity assuming RH = 80%. We define the following simulations:

- A base simulation $\mathcal{B}$, intended to represent the preindustrial polar climate, with CO_2 = 280 ppm, T_0^{in} = 0°C (the observed annual-mean surface temperature at around 60°N), F_s = 50 W m^{-2} (roughly the annual-mean absorbed surface solar radiation averaged over the cap poleward of 60°N), and τ = 10 days.

- A perturbed simulation $\mathcal{P}$, intended to represent the effects of a global doubling of CO_2, with CO_2 = 560 ppm and T_0^{in} increased by 3 K from the base state, consistent with central estimates of global climate sensitivity to a doubling of CO_2. Changes in surface heat source F_s are a proxy for sea ice feedback in this model. For guidance, Arctic surface albedo feedback is estimated at ~3 W m^{-2} per K of global warming in climate models (Andry et al. 2017), suggesting ΔF_s = 10 W m^{-2} is an appropriate round-number value for this perturbation. Changes in τ depend on subtle changes in atmospheric dynamics which are difficult to specify a priori, so we simply leave it unchanged.

- A set of single-perturbation simulations $\{\mathcal{P}_{\text{in}}, \mathcal{P}_s, \mathcal{P}_{CO_2}, \mathcal{P}_q\}$ where the perturbations of $\mathcal{P}$ are applied one at a time. These simulations are intended to provide a forcing-feedback decomposition of the change from $\mathcal{B}$ to $\mathcal{P}$, as done in Henry et al. (2021). They are conducted with humidity held fixed: in $\mathcal{P}_{CO_2}$, $\mathcal{P}_{\text{in}}$, and $\mathcal{P}_s$ the temperature is allowed to respond to increased CO_2, T_e^{in}, and F_s respectively, but q is held fixed at its value in $\mathcal{B}$. To evaluate the water vapor feedback, $\mathcal{P}_q$ has humidity fixed at its value in $\mathcal{P}$. Water vapor plays a dual role in the model, affecting both radiative cooling Q_{rad} and latent heating Q_{lat}. These roles are decoupled in the partial perturbation runs: humidity is fixed only the radiation component, so as to isolate the purely radiative water vapor feedback.

d. Testing the model against reanalysis

To test the model's skill in reproducing observed temperature and heating profiles, we define a simulation aimed to capture the modern Arctic climate. This simulation is identical to the base simulation $\mathcal{B}$ above, except that T_e^{in} and τ are taken from reanalysis (profiles shown in Figure 1a,b), and CO_2 is set to 370 ppm, a typical value for the 1980-2018 period covered by the reanalysis data.

Results for this observationally-informed simulation are shown by dashed lines in Figure 1, where they can be directly compared with corresponding reanalysis climatologies (solid lines). In view of the model's simplicity, its match to the data is surprisingly good. It reproduces the structure and magnitude of the temperature profile with good accuracy (Figure 1a), except near the surface where it overpredicts the intensity of the surface inversion and makes surface temperature too cold. It also gives a good match to the advective heating rate (Figure 1c), in particular capturing the location of peak heating at around 900 hPa and its decline below that level—note that this is also the region where the ventilation timescale shows a sharp increase (Figure 1b). Perhaps most surprisingly, the model also captures the partitioning between dry and latent heating quantitatively well (Figure 1d), despite its very simple treatment of condensation. We note also that the good match to observations provides a posteriori justification for the neglect of eddy vertical transport in the derivation of Eq. (7).

3. The surface radiator fin

Results for the base simulation $\mathcal{B}$ are shown by solid lines in Figure 2. The diabatic cooling rate (blue line in Figure 2b) has a bottom-heavy structure, with a strong peak at the surface. This bottom-amplified cooling rate structure makes the column temperature profile more stable than the inflow temperature T^{in} throughout the troposphere, and an inversion develops near the surface (Figure 2a).

The advective heating rate profile (red line in Figure 2b) is just the mirror image of the cooling rate: air parcels experience greatest cooling and converge most energy where the cooling rate is strongest. The profile is qualitatively similar to that of the winter Arctic diagnosed from reanalysis (Figure 1c), except that in reanalysis it peaks around 900 hPa instead of at the surface. We attribute this difference to the different profile of the ventilation timescale τ, which is vertically uniform in this simulation but peaks strongly near the surface in reanalysis (Figure 1b). Winds are more sluggish near the surface and tend to recirculate around the Arctic (Papritz et al. 2023), reducing the rate of energy convergence. The difference is not crucial, however; we have repeated all the simulations described in this paper using the reanalysis τ profile and find no qualitative change in our results.

Separating the diabatic cooling rate into its radiative and diffusive components (Figure 2c) shows the latter contributes strongly to the surface peak, giving the impression that diffusion is essential in creating the temperature inversion. This is not the case, however: repeating simulation $\mathcal{B}$ with diffusion deactivated (dashed lines in Figure 2) shows radiative cooling increasing to replace the lost diffusive cooling. Total diabatic cooling remains essentially unchanged, and the temperature inversion persists albeit with a much larger surface discontinuity. This interchangeability between radiative and turbulent fluxes implies that the temperature inversion is a fundamental feature of the polar climate, independent from the details of atmospheric energy transfer.

The ultimate cause of the temperature inversion is the intrinsic thermodynamic disequilibrium between atmosphere and surface in the polar climate. Because the atmosphere is optically thin while the surface is opaque, the surface can cool strongly by direct emission to space; this has long been recognized as the basic reason for the existence of transient surface-based inversions in polar regions (Wexler 1936; Curry 1983). If surface cooling is climatologically balanced only by the weak polar insolation, the result is a steady-state surface temperature much colder than the air flowing in from lower latitudes. Basic thermodynamics dictates that this disequilibrium will generate downward energy fluxes from the atmosphere to the surface, which will warm the surface and cool the atmosphere but cannot make the surface warmer than the atmosphere and cannot remove the temperature inversion. The term *radiator fin* has been used in climate science to describe a situation where one part of the atmosphere is cooled by energy transfer to another part—the radiator fin—where it can be efficiently emitted to space (Pierrehumbert 1995). In this sense, the surface serves as a radiator fin for the lower atmosphere.

To make this picture quantitative, we first separate the atmospheric longwave radiative flux into two streams. One, denoted F_{atm}, consists of radiation absorbed and emitted by the atmosphere and is responsible for atmospheric radiative cooling. The other, denoted F_{win}, consists of radiation emitted by the surface which travels through the atmosphere with no interaction, largely in the wavelength range containing the water vapor window. Profiles of the two streams, along with the turbulent energy flux denoted F_{dif}, are shown in Figure 3a.

Under the dry, clear-sky conditions of this simulation, F_{win} is large and accounts for almost half of the outgoing longwave radiation. Only F_{atm} and F_{dif} contribute to atmospheric cooling and to atmosphere-surface energy exchange. F_{atm} is everywhere upward while F_{dif} is downward; their sum

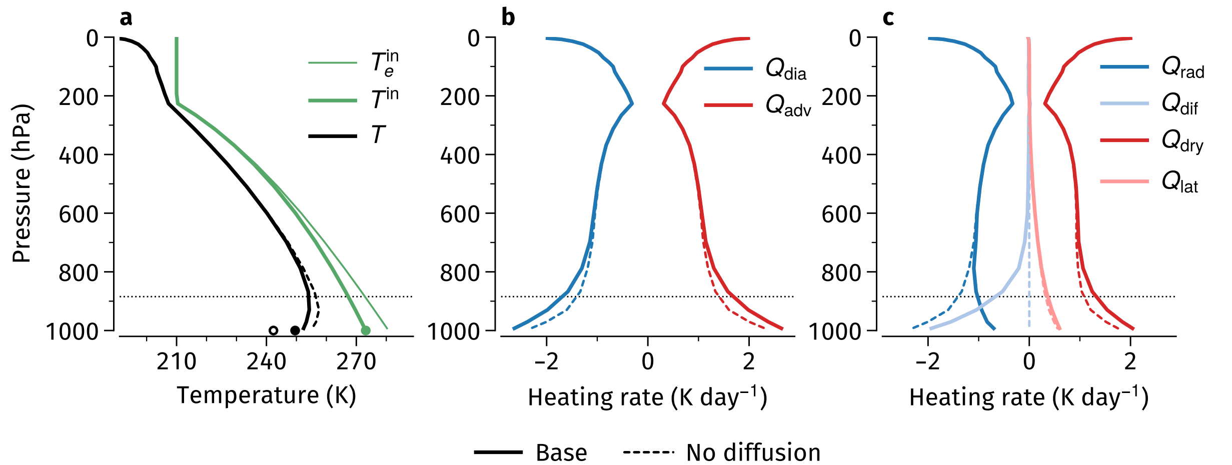

FIG. 2. (a) Temperature and (b,c) heating/cooling rate profiles in the base simulation $\mathcal{B}$, as indicated by the legend in each panel (solid lines). Dashed lines show results for simulation $\mathcal{B}$ performed with zero diffusivity. In (a), black dots show surface temperature in the standard (filled) and no-diffusion case (hollow), green dot shows surface inflow temperature T_0^{in}. Thin dotted lines indicate the zero-flux level.

crosses zero around 900 hPa, with net downward energy transport below this level. The zero-flux level coincides with the top of the temperature inversion (dotted line in Figure 2a), implying that the inversion layer is where the atmosphere is cooling primarily by energy transfer to the surface, rather than to space. Note that exactly the same result is obtained in the no-diffusion case, except that the downward flux to the surface is entirely carried by radiation (dashed lines in Figure 3a).

The surface energy budget (Figure 3b) shows that the surface extracts a total of 27 W m^{-2} from the atmosphere, which it then emits directly to space through F_{win} (together with 50 W m^{-2} from the surface heat source F_s), confirming the radiator fin picture. The radiator fin is not a large contributor to the total atmospheric energy budget, however, which is dominated by 113 W m^{-2} in dry atmospheric energy transport AHT$_{\mathrm{dry}}$, defined as

$$\mathrm{AHT}_{\mathrm{dry}} = \frac{c_p}{g} \int_0^{p_s} Q_{\mathrm{dry}}\, dp, \tag{12}$$

and a smaller contribution from moist transport AHT$_{\mathrm{moist}}$ (defined similarly but with Q_{lat} replacing Q_{dry}), which are mostly balanced by 102 W m^{-2} emission to space. Nonetheless, the radiator fin

TABLE 1. Effective water vapor window width w and disequilibrium D (Eq. 13) in the base simulation (first column), and their change in perturbed simulations (remaining columns).

	$\mathcal{B}$	$\mathcal{P}_{\mathrm{in}}$	$\mathcal{P}_s$	$\mathcal{P}_{\mathrm{CO_2}}$	$\mathcal{P}_q$	$\mathcal{P}$
w	0.35	0.00	0.00	−0.01	−0.02	−0.03
D (K)	44	5	−10	−2	−3	−10

acts on a shallow layer and drives strong cooling there, and is essential in controlling the strength of the temperature inversion.

To give a quantitative measure for the strength of the radiator fin effect, we define a surface temperature T_s^* which would balance the surface heat source F_s in the absence of warming by energy transfer from the atmosphere: $w\sigma T_s^{*4} = F_s$, where w is the fraction of the surface upward radiation emitted directly to space and measures the effective width of the water vapor window. We can then define a temperature difference

$$D = \langle T_e^{\mathrm{in}} \rangle - T_s^* = \langle T_e^{\mathrm{in}} \rangle - \left(\frac{F_s}{w\sigma} \right)^{1/4} \tag{13}$$

where $\langle \cdot \rangle$ is an average over the 900–1000 hPa layer. D gives a bulk measure of the thermodynamic disequilibrium discussed earlier in this section. Values of w and D are given in Table 1, with w diagnosed as $F_{\mathrm{win}}/\sigma T_s^4$. The diagnosed magnitude of the window width w of 0.35 is comparable to Cronin and Jansen (2016)'s suggested 0.25 for clear-sky conditions, and the disequilibrium D of 44 K is approximately double the model's contrast between equilibrated surface temperature ≈ 250 K and the inflow temperature ≈ 270 K. We expect that perturbations that increase the disequilibrium, such as a warming of the inflow, will increase the strength of the inversion, while an increase in F_s or a narrowing of the water vapor window will weaken the inversion. These expectations are tested in the next section.

4. Response to perturbations

a. Lapse rate

When the base state $\mathcal{B}$ is perturbed by a simultaneous increase of T^{in}, $\mathrm{CO_2}$, and F_s to yield the perturbed state $\mathcal{P}$, the temperature profile warms throughout the troposphere and cools in the

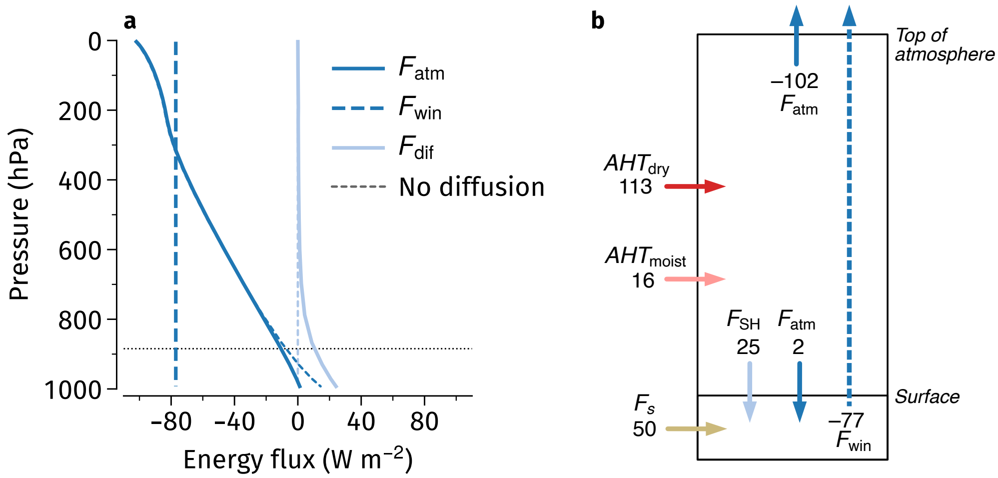

Fig. 3. (a) Radiative and diffusive energy fluxes, defined positive downwards, in the base simulation $\mathcal{B}$ (solid and thick dashed lines, see text for definitions). Thin dashed lines show the corresponding fluxes in the no-diffusion simulation. (b) Column energy budget in $\mathcal{B}$. All fluxes in W m^{-2}, vertical fluxes defined positive downward.

stratosphere (Figure 4e). The warming has a bottom-heavy structure, with lapse rate increasing strongly near the surface and more weakly at upper levels. Comparing this response to the change in inflow temperature T^{in} (thick green line) gives a measure of the polar amplification between midlatitudes and the pole. Polar amplification is strong in the lower troposphere but negative at upper levels, where the pole warms less than midlatitudes. All these features agree with the results of comprehensive climate models subject to global forcing (Previdi et al. 2021; Taylor et al. 2022),

To understand the origins of this general destratification of the polar atmosphere, we examine the single-perturbation simulations $\mathcal{P}_{\text{in}}$, $\mathcal{P}_s$, $\mathcal{P}_{\text{CO}_2}$ and $\mathcal{P}_q$. They provide a forcing-feedback decomposition of the total response with near-zero residual (dashed line in Figure 4e), implying the decomposition is almost perfectly linear. In the following paragraphs we examine each of the perturbations in turn, starting with the response to increased surface heat source ($\mathcal{P}_s$), moving on to greenhouse gases ($\mathcal{P}_{\text{CO}_2}$ and $\mathcal{P}_q$), and ending with the response to inflow warming ($\mathcal{P}_{\text{in}}$).

The temperature response to increased F_s is strongly bottom-amplified in the lower troposphere and negligible above ~600 hPa (Figure 4b), implying a strong reduction in inversion strength and confirming our expectations based on the radiator fin picture of the previous section: increasing F_s

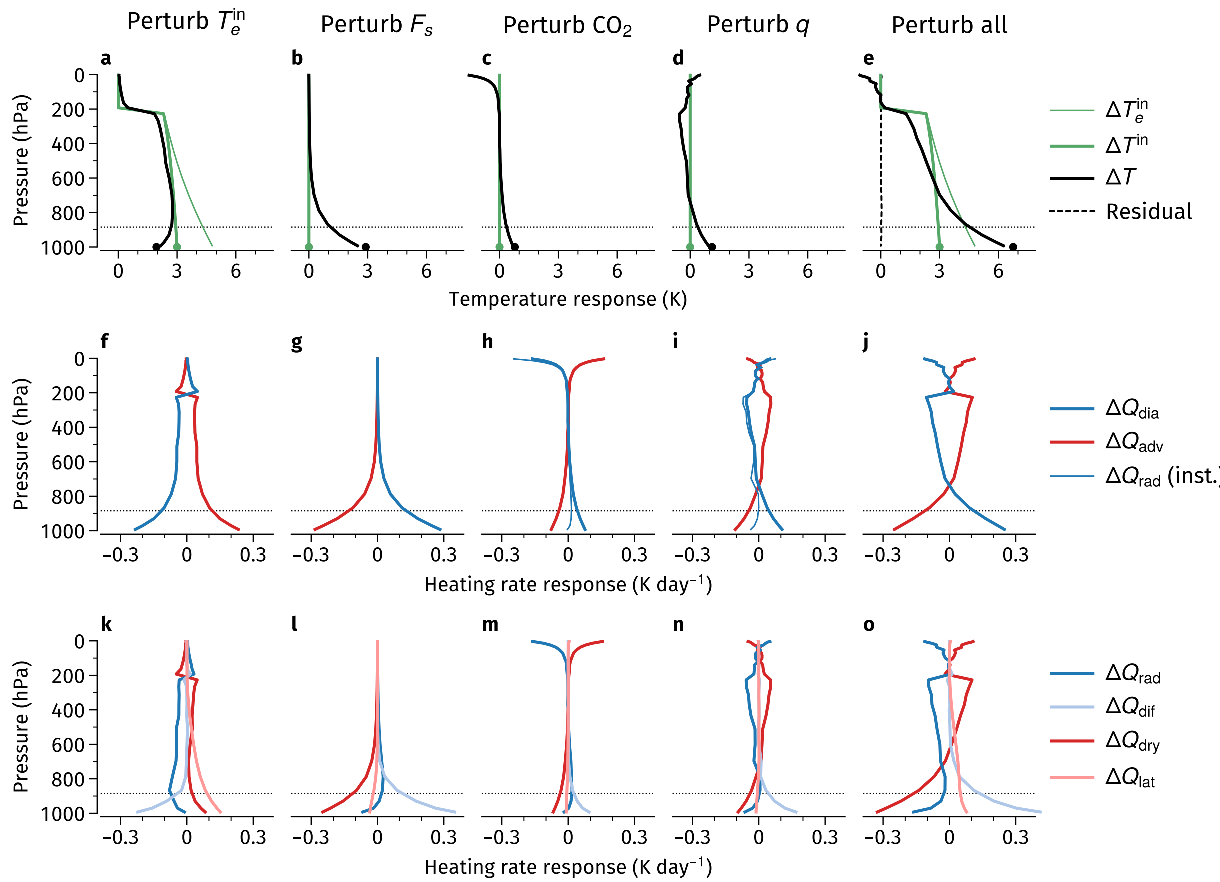

FIG. 4. Changes in temperature (top row) and heating/cooling rates (middle and bottom rows) from base simulation $\mathcal{B}$ to perturbed simulation $\mathcal{P}_{in}$ (first column), $\mathcal{P}_s$ (second column), $\mathcal{P}_{CO_2}$ (third column), $\mathcal{P}_q$ (fourth column) and $\mathcal{P}$ (fifth column). Dots in top row show surface temperature change in the inflow (green) and in the column (black). Dashed line in (e) shows the residual between the sum of individual responses in (a-d) and the full response in $\mathcal{P}$. Thin blue lines in (h,i) show the instantaneous response of the radiative cooling rate when the corresponding perturbation is applied. Thin dotted lines indicate the zero-flux level of the base simulation.

reduces atmosphere-surface disequilibrium D by 10 K (Table 1). Physically, air masses entering the polar cap now encounter a warmer surface, experience weaker diabatic cooling as they traverse the cap (Figure 4g), and therefore remain warmer. This effect is strongest in the inversion layer below the zero-flux level, which is directly coupled to the surface, but is communicated some distance upward by intra-atmospheric radiative and diffusive energy exchange. The upper troposphere experiences no forcing and remains unaffected. Reduced energy transfer from atmosphere to surface also implies an *upward* anomaly in surface radiative and turbulent fluxes (Figure 5g).

Turning to greenhouse gas forcing in $\mathcal{P}_{CO_2}$ and $\mathcal{P}_q$ (Figure 4c,d), we see in both cases a bottom-amplified structure similar to that in $\mathcal{P}_s$, at least in the near-surface layer. The instantaneous effect of increasing either CO_2 or H_2O concentrations is to render previously transparent wavelengths opaque, blocking direct surface emission to space within a certain wavelength range (Jeevanjee et al. 2021; Seeley and Jeevanjee 2021; Koll et al. 2023). The result is an effective narrowing of the water vapor window. This leads to an instantaneous decrease in surface cooling by F_{win} (Figure 5c,d) and thus a warming tendency on the surface (consistent with a surface vs. atmosphere decomposition of reanalysis-based CO_2 forcing for Earth's Arctic, Chen et al. 2023, their Figs. 10a,b). Hence the similarity between the response to greenhouse gases and to direct surface warming by F_s: they both weaken D (Table 1), making the surface radiator fin less efficient albeit by different mechanisms.

Differently from F_s, however, increased water vapor and CO_2 provide strong cooling responses in the free troposphere and stratosphere respectively (Fig. 4c,d; 'free troposphere' here refers to the layer between ~800 and 300 hPa). Increased CO_2 shifts radiative emission to space from the surface to the stratosphere within a wavelength range on the flanks of the main 15 micron absorption band, causing increased cooling in the stratosphere (Jeevanjee et al. 2021; Chen et al. 2024). Increased humidity produces cooling in the upper troposphere. The interpretation is more subtle in this case. H_2O produces radiative cooling to space throughout the troposphere, but the exponential decay of humidity with height implies an abrupt decline of this cooling ability above a height where the water path drops below a critical level (the upper-tropospheric "kink", Jeevanjee and Fueglistaler 2020). This behavior can clearly be seen in Fig. 2c, which shows fairly uniform radiative cooling rates between 800 and 400 hPa and a sharp decrease towards the tropopause at around 250 hPa. The effect of increasing water vapor is to shift this profile upwards, yielding increased cooling rates in the 250–400 hPa layer. This effect is of some importance since it emerges as a key cause of free-tropospheric lapse rate change and of negative upper-level polar amplification, and would be worth exploring further with a more accurate radiative scheme than employed here. The gray-radiation based theory of Cronin and Jansen (2016) also produces a bottom-amplified temperature response to increased atmospheric opacity, but this spectrally-informed picture is more faithful to the balances at upper levels.

Finally, we examine the response to increased T_e^{in}. The entire troposphere warms in this case (Figure 4a). Since the T_e^{in} perturbation is itself bottom-heavy (because of greater humidity at

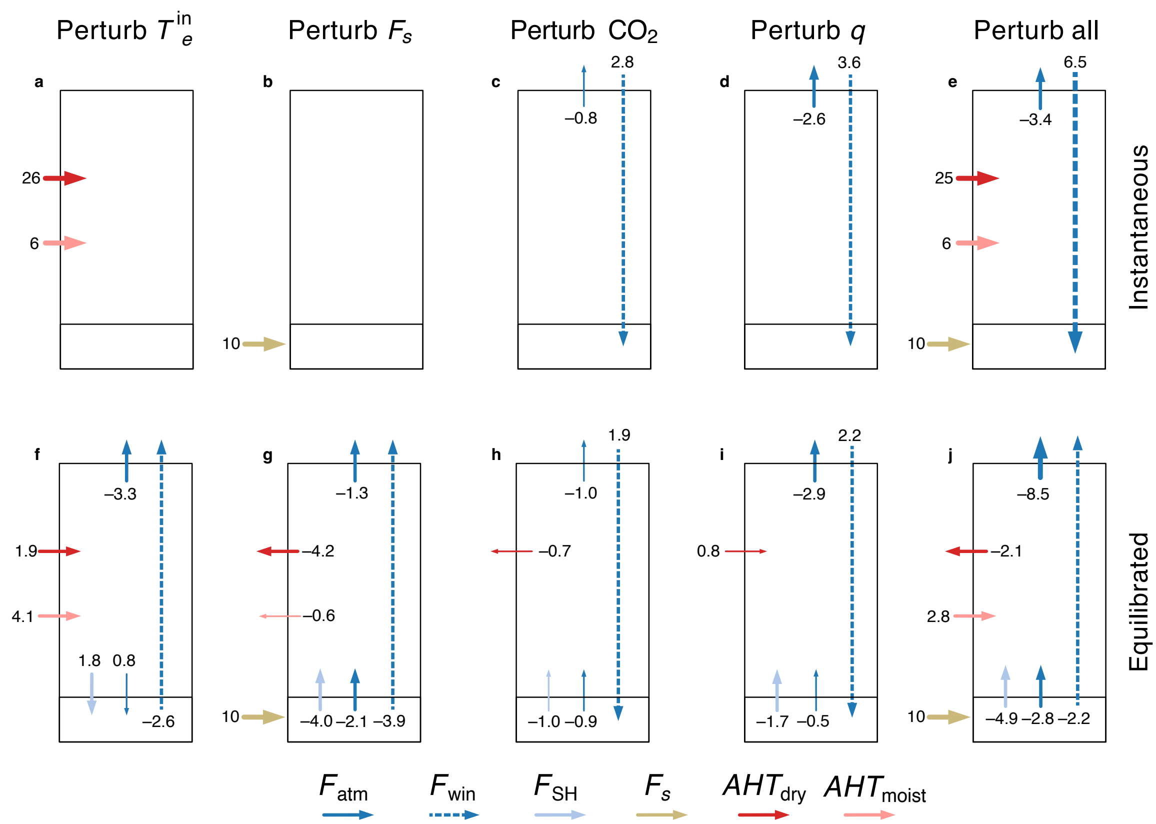

FIG. 5. Instantaneous (top row) and equilibrated (bottom row) perturbation energy budget for the change from base simulation $\mathcal{B}$ to perturbed simulation $\mathcal{P}_{\mathrm{in}}$ (first column), $\mathcal{P}_s$ (second column), $\mathcal{P}_{CO_2}$ (third column), $\mathcal{P}_q$ (fourth column) and $\mathcal{P}$ (fifth column). Thick arrows show changes >1 W m^{-2}, thin arrows <1 W m^{-2}. Changes <0.5 W m^{-2} are omitted for clarity.

low levels), and since the model essentially relaxes T to T_e^{in} (see Section 2b), we expect to see a similar bottom-heavy structure in the T response. This is indeed the case in the free troposphere, where the lapse rate increases somewhat. Upper-tropospheric warming also leads to increased atmospheric cooling to space (top-of-atmosphere F_{atm} increases by 3.3 W m^{-2}, Figure 5f). On the other hand, atmosphere-surface disequilibrium increases, enhancing the surface peak in diabatic cooling (Figure 4f) and strengthening the inversion (Figure 4a). Warming of the inflow increases the stratification the lower troposphere, counteracting the destratifying effect of the other perturbations.

Equivalently, this 'forcing' is not polar amplified at the surface, with ≈ 2 K warming compared to the imposed 3 K change in T^{in}.

b. Dry and moist energy convergence

A robust result of climate model simulations subject to global radiative forcing is that changes in vertically-integrated dry and moist energy transport to the poles compensate each other, yielding near-zero net change in transport (Hwang et al. 2011). This compensation is understood to result from opposite changes in temperature and moisture gradients: despite polar amplification, Clausius-Clapeyron scaling means moisture increases more in midlatitudes than at the poles, so moist transport increases while dry transport drops (Merlis and Henry 2018; Armour et al. 2019). This compensation also occurs in our all-perturbations simulation $\mathcal{P}$, where a +2.8 W m^{-2} change in vertically-integrated moist transport is offset by a -2.1 W m^{-2} change in dry transport (Figure 5j). In the rest of this section, we study how different forcings and feedbacks, and different layers in the atmospheric column, contribute to this overall compensation.

To provide a framework for this discussion, we use (9) and (10) to write the steady-state perturbation energy budget as

$$\frac{1}{\tau}(\Delta T^{\text{in}} - \Delta T) \; + \; \frac{1}{\tau}(\alpha^{\text{in}}\Delta T^{\text{in}} - \alpha\Delta T) \; = \; -\Delta Q_{\text{dia}} \tag{14}$$

where we have defined the Clausius-Clapeyron factor

$$\alpha(T) = \frac{\ell_v \text{RH}}{c_p} \left. \frac{dq_{\text{sat}}}{dT} \right|_T \tag{15}$$

and $\alpha^{\text{in}} = \alpha(T^{\text{in}})$. As shown in Figure 6a, $\alpha \approx 1$ at 270 K and drops by an order of magnitude for every $\sim$20 K drop in temperature.

In the upper troposphere, base-state temperatures are below 250 K (Figure 2), and both α and $\alpha^{\text{in}} \ll 1$. Moisture plays a negligible role, and changes in diabatic heating are entirely balanced by dry heating: specifically, dry heating increases to balance increased radiative cooling in $\mathcal{P}_{\text{in}}$ and $\mathcal{P}_q$ (Figure 4k,n). Physically, increased radiative cooling causes a larger temperature drop from inflow to outflow, increasing the dry energy convergence.

In the lower troposphere, on the other hand, $\alpha \ll 1$ but $\alpha^{\text{in}} \sim 1$. In $\mathcal{P}_s$, $\mathcal{P}_q$ and $\mathcal{P}_{\text{CO}_2}$ there is no T_e^{in} perturbation, so (14) reduces to $\Delta T/\tau \approx \Delta Q_{\text{dia}}$ and decreased diabatic cooling is again balanced almost entirely by reduced dry heating (Figure 4 l,m,n). Physically, these perturbations warm the surface and reduce the radiator fin effect. The resulting drop in diabatic cooling results in warmer outflow temperature and reduced dry convergence, but outflow humidity is hardly affected by the warming so there is little change in moist convergence. In $\mathcal{P}_{\text{in}}$, however, (14) becomes $(\Delta T^{\text{in}} - \Delta T)/\tau + \alpha^{\text{in}}\Delta T^{\text{in}} \approx -\Delta Q_{\text{dia}}$. In this case, increased latent heating balances much of the increase in diabatic cooling (Figure 4k). Physically, increased inflow temperature increases the radiator fin effect; the resulting increase in diabatic cooling mostly consumes the increased latent heat of the inflow air, however, leading to a modest change in inflow-to-outflow temperature drop and hence in dry advective heating rate.

When added together (Figure 4o), the perturbations give free-tropospheric increase but lower-tropospheric decrease in dry heating, along with lower-tropospheric increase in latent heating (contributed entirely by the T_e^{in} perturbation). The vertically-integrated compensation between dry and moist transports is thus a delicate balance between positive and negative changes at different levels in the column responding to different physical processes. There is no obvious constraint imposing exact compensation. It is therefore not surprising that the degree of compensation is highly variable between climate models (Hwang et al. 2011; Hahn et al. 2021), which have varying F_s or T^{in} in our framework. Note also that the layer-wise compensation seen in the RAE single-colum model cannot be captured in energy balance models, which parameterize all transport down moist- or dry-energy gradients based on surface temperature only (e.g., Feldl and Merlis 2021; Chang and Merlis 2022).

Moreover, the degree of compensation is sensitive to the surface heat source perturbation ΔF_s. If we repeat simulation $\mathcal{P}$ but varying ΔF_s in the range 0–50 W m^{-2}, we find that dry transport decreases strongly while moist transport stays roughly constant as ΔF_s increases (Figure 6b). This happens because the negative contribution to dry heating given by the F_s perturbation grows while leaving latent heating largely unaffected (Figure 4l). Recalling that ΔF_s represents sea ice feedback in our model, we note that this result provides an explanation for the negative correlation between the strength of surface albedo feedback and atmospheric energy transport in climate model intercomparisons (Pithan and Mauritsen 2014; Hahn et al. 2021, their Figure 6).

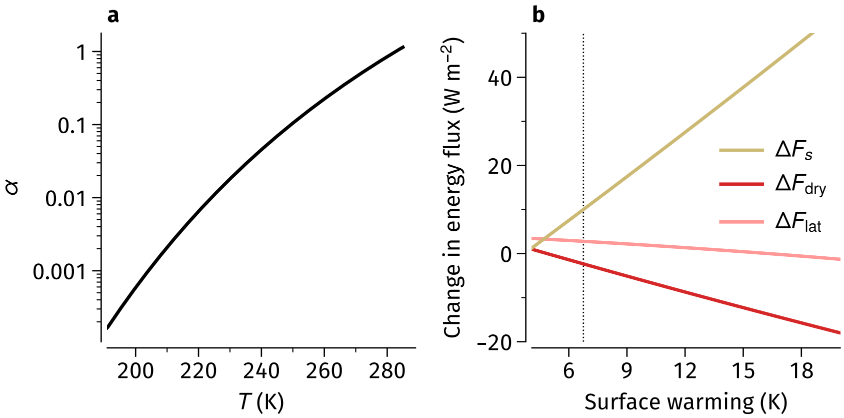

FIG. 6. (a) Behavior of the non-dimensional Clausius-Clapeyron factor α (see Eq. 15) as a function of temperature, assuming RH=80% and a pressure of 1000 hPa. (b) Behavior of the dry and moist advective heating perturbations in response to changing surface heat source perturbation, plotted as a function of surface warming.

5. Local and remote contributions to polar warming

Polar warming is driven by a combination of remote and local forcing, both amplified by local feedbacks (Screen et al. 2012; Stuecker et al. 2018; Park et al. 2018; Henry et al. 2021). Here, we partition the total warming seen in the all-perturbations simulation $\mathcal{P}$ into remote and local contributions. Remote forcing in our model is encapsulated in the T_e^{in} perturbation. We take the remote warming contribution to be the sum of the direct response to this forcing (given by simulation $\mathcal{P}_{\mathrm{in}}$), and the portion of the water vapor feedback driven by remote warming (Henry et al. 2021). We quantify this portion by performing an additional simulation identical to $\mathcal{P}_{\mathrm{in}}$ but allowing water vapor to adjust interactively at fixed RH. Local forcing is provided by the CO_2 and F_s perturbations, both amplified by corresponding portions of the water vapor feedback (again quantified by additional simulations). The F_s perturbation can be seen as this model's representation of sea ice feedback, which could be partly driven by remote warming. Nonetheless, we treat F_s as a purely local effect for consistency with previous work (Henry et al. 2021), while recognizing that this assumption overestimates the local contribution to total warming.

Results are presented in Figure 7. Partitioning of the water vapor feedback shows that it is almost entirely due to remote warming (Figure 7a), presumably because this warming is deep and promotes enhanced humidity throughout the column rather than in a near-surface layer. (Consistently with this argument, we also note that water vapor radiative kernels have small or even negative near-surface values in the Arctic because of the climatological inversion, implying modest changes in outgoing longwave radiation for increased near-surface specific humidity (Soden et al. 2008; Kim et al. 2021).) Despite this contribution from water vapor feedback, the surface warming attributed to remote forcing remains smaller than that attributed to local forcing by about 1 K (Figure 7b). This differs from the results of regionally-forced climate model simulations, which show almost equal remote- and locally-driven warmings (Stuecker et al. 2018; Semmler et al. 2020). This difference is likely due to our attribution of the F_s contribution entirely to local forcing. Nonetheless, our results confirm that remote forcing plays a key role in driving strong polar amplification: if remote forcing had no effect on the poles, there would be very weak polar amplification.

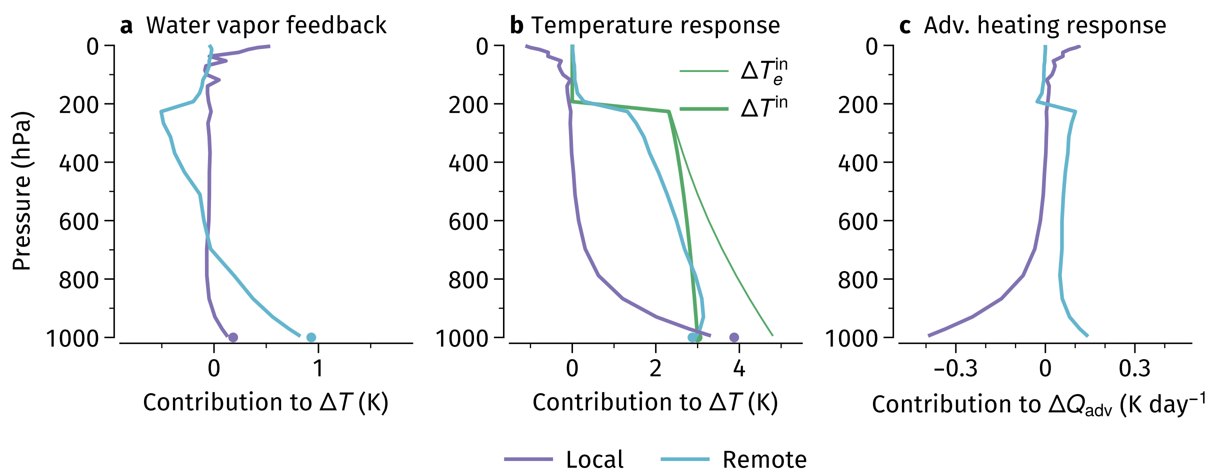

FIG. 7. Decomposition of the (a) radiative water vapor feedback, (b) total temperature response, and (c) advective heating rate response into contributions due to local and remote forcings/feedbacks.

Remote forcing also drives increased advective heating—and therefore increased diabatic cooling—throughout the troposphere, while local forcing is responsible for the net drop in advective heating in the lower troposphere (Figure 7c). This result is consistent with and helps interpret the findings in Audette et al. (2021), who examine the response of atmospheric energy transport and moist-isentropic circulation in atmospheric models subject to changing surface conditions. They find that remote sea-surface temperature warming leads to greater energy transport to the Arctic and greater isentropic mass flux. Both are consistent with the remote response in Figure 7c—note in fact that the poles constitute the subsiding branch of the isentropic circulation (Pauluis et al. 2010), and in isentropic coordinates subsidence is equal to the diabatic cooling rate and related moisture loss by precipitation (it is simply the transformation of air masses from higher to lower entropy or MSE classes). This isentropic picture also forms the basis of a feedback analysis suitable to separating the distinctive upper- vs. lower-tropospheric warming contributions in the Arctic (Feldl et al. 2020). Audette et al. (2021) further show that local polar forcing by reduced sea ice cover drives reduced energy transport and a weakening of the isentropic mass transport in the lower troposphere; both are again consistent with our results for local forcing, for the same physical reasons. Moreover, they attribute this reduction in energy transport to warming of the low-level outflow from the Arctic, consistent with the air-mass transformation perspective discussed in Section 3b. In summary, our single-column model results suggest that changes in poleward energy transport and in isentropic mass flux are just two sides of the same coin.

6. Sensitivity to surface elevation: The Antarctic case

Polar amplification is hemispherically asymmetric, being stronger over the Arctic than over Antarctica. This asymmetry has been attributed in part to Antarctica's high elevation: climate model simulations in which Antarctica is flattened with no change in surface albedo show substantially increased polar amplification (Salzmann 2017; Hahn et al. 2020).

This issue provides a useful test case for the single-column model and for the physical picture developed in Sections 3 and 4. We perform a series of simulations identical to $\mathcal{B}$ but with varying surface pressure. The T_e^{in} profile prescribed in these simulations is identical to the portion of the T_e^{in} profile of $\mathcal{B}$ that is above the surface. The resulting series of base-state temperature profiles is shown in Figure 8a. In agreement with Hahn et al. (2020), the surface inversion becomes stronger but shallower as the surface pressure decreases.

We then perform a corresponding series of perturbed simulations which are identical to $\mathcal{P}$ with one exception: the surface heat source perturbation $\Delta F_s = 0$ in all cases, to mimic no change in surface albedo. Profiles of temperature change from corresponding base states are shown in Figure 8b. The lapse rate increases roughly uniformly throughout the column in these simulations, without the lower-tropospheric enhancement seen in $\mathcal{P}$ (Figure 4e). The reason is that without an F_s perturbation, the reduction in atmosphere-surface disequilibrium D due to greenhouse gases roughly cancels out the increase due to T_e^{in} (Figure 8c). There is therefore little change in radiator fin strength, implying that near-surface lapse-rate changes in these simulations are not primarily

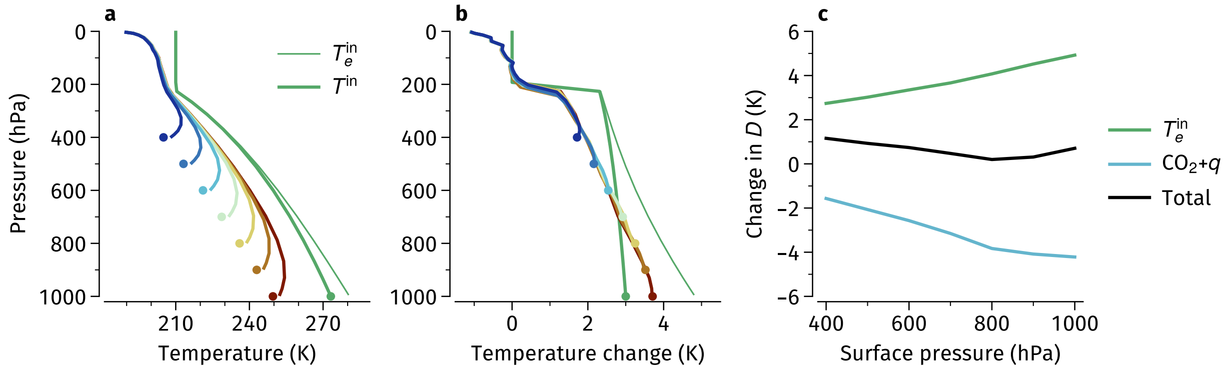

FIG. 8. (a) Base-state temperatures and (b) temperature response to perturbed T_e^{in} and CO_2 for simulations with varying surface pressure. Dots show surface temperature, plotted at the corresponding value of surface pressure. (c) Change in atmosphere-surface disequilibrium D from the base to the perturbed simulations as a function of surface pressure (black line), and its partitioning into contributions from increased T_e^{in} and in greenhouse gases.

due to the boundary-layer processes that control the surface inversion strength. Instead, lapse-rate changes are driven by relaxation towards the bottom-amplified T_e^{in} perturbation—note that the T perturbation profile is roughly parallel to that of T_e^{in} in Figure 8b—and by upper-tropospheric cooling by water vapor as discussed in Section 4a.

In summary, these results show that the model's surface temperature response decreases with increasing surface elevation, in agreement with the climate model results of Salzmann (2017) and Hahn et al. (2020). Our physical interpretation is different from theirs, however, and points to the importance of lower-tropospheric latent heat release in yielding a bottom-amplified temperature response which enhances polar amplification.

7. Comparison with other forcing-feedback decompositions

Here we compare the forcing-feedback decomposition provided by our relaxation approach with alternative decompositions provided by the fixed-heating RAE approach (Henry et al. 2021) and by the conventional TOA decomposition. For the fixed-heating approach, we perform simulations with the same parameter settings specified in Section 2c, but prescribing a fixed advective heating rate diagnosed from simulations $\mathcal{B}$ and $\mathcal{P}$. For the TOA decomposition, we use the partial radiative perturbation method (Colman et al. 2001): using the radiative transfer code offline, we compute the TOA radiative perturbation caused by replacing temperature, humidity and CO_2 values in $\mathcal{B}$ with those from $\mathcal{P}$ one at a time; we then divide by the Planck feedback to obtain as surface temperature change contribution from each feedback. Contributions from changes in surface heat source and atmospheric heat transport are computed by dividing ΔF_s and vertically-integrated ΔQ_{adv} by the Planck feedback.

Results are presented in Figure 9. Temperature responses to F_s, CO_2 and q in the fixed-heating approach are qualitatively similar to those in the relaxation approach, but with much greater amplitude: since advective heating is not allowed to adjust, changes in diabatic cooling must be entirely compensated by large temperature changes. Note in particular that the response to F_s is positive all the way into the stratosphere in the fixed-heating approach. Moreover, the negative lower-tropospheric lobe of ΔQ_{adv} (shown in Figure 4j) yields a large negative temperature perturbation even at the surface, although vertically-integrated atmospheric heat transport actually increases. These responses appear more difficult to interpret physically than in the relaxation approach.

The TOA decomposition (Figure 9c) shows the largest contribution to surface temperature change is from F_s, followed by lapse-rate feedback, while other terms play a smaller role; in particular, atmospheric transport gives a small positive contribution. This is qualitatively consistent with the relative roles of Arctic surface albedo, lapse-rate and atmospheric transport feedbacks in diagnosed in climate models (Pithan and Mauritsen 2014; Hahn et al. 2021). ΔF_s is also the largest contributor in the relaxation and fixed-heating approaches, though it is much larger in the fixed-heating approach to compensate for the negative contribution from advective heating (recall from Section 4b that ΔF_s drives the largest reduction in Q_{adv}). The two RAE approaches do not have an explicit lapse-rate feedback contribution since it is implicitly partitioned among the other contributions, making the CO_2 and q contributions larger than in the TOA approach. In addition, the relaxation approach has no separate atmospheric transport feedback; instead it has a substantial contribution from ΔT_e^{in}, which we consider a forcing, while changes in atmospheric energy convergence are partitioned among all four contributions.

8. Summary and conclusions

We have developed a single-column model for clear-sky RAE in which heating by lateral energy advection is represented as a relaxation toward a fixed midlatitude profile of temperature and

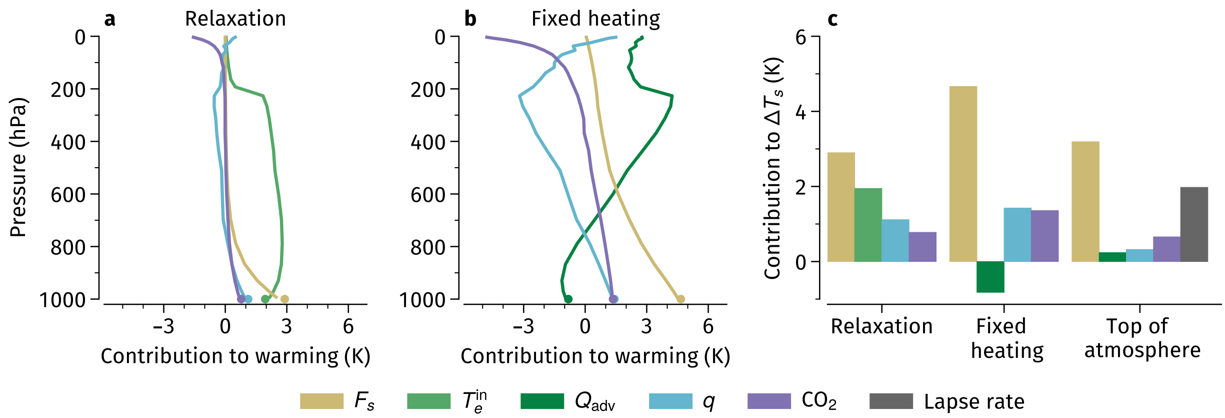

FIG. 9. Temperature responses to individual perturbations in the (a) relaxation and (b) fixed-heating approaches, and (c) contributions to surface temperature change according to the three decompositions. Dots in (a,b) show surface temperature change.

humidity, encapsulated in the equivalent temperature profile T_e^{in}. Despite its simplicity, the model is able to adequately reproduced observed Arctic temperature and energy convergence profiles. Analysis of the model's steady-state energy balance, schematized in Figure 10a, and its response to a global-warming-like perturbation (Figure 10b), allows us to provide some answers to the key questions posed in the Introduction:

1. *Why is there a climatological surface-based inversion, and what mechanisms control the polar lapse-rate response to global warming?*

   The essential reason for the existence of a climatological surface temperature inversion is the thermodynamic imbalance between the relatively warm air flowing into the polar cap and the cold surface temperature that results from strong surface cooling to space through the water-vapor window. As a result, the lower troposphere cools strongly to the surface; this cooling can be mediated by radiative or turbulent fluxes interchangeably, but necessitates a surface temperature inversion in either case. We refer to this surface cooling mechanisms as the surface radiator fin.

   Changing inversion strength in response to global-warming-like perturbations can be readily predicted by thinking about their effects on the surface radiator fin. All else equal, a warming of incoming air will increase thermodynamic imbalance and strengthen the radiator fin, leading

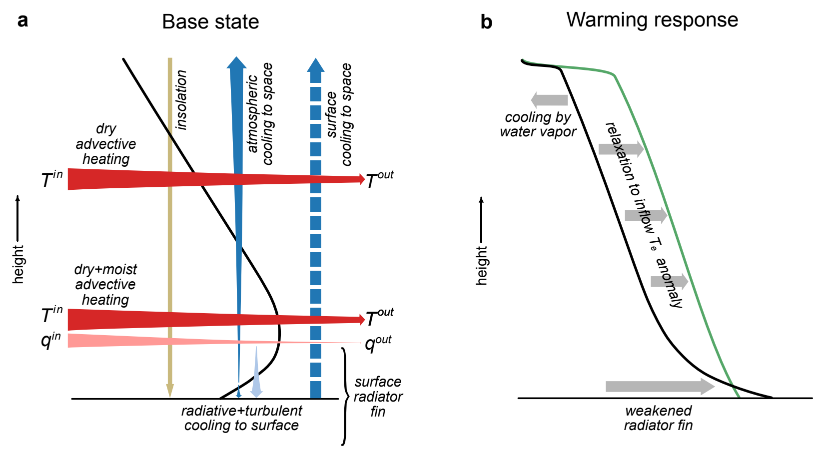

FIG. 10. Schematics summarizing (a) the energy balances involved in the maintenance of the base state, and (b) the mechanisms controlling polar lapse rate response to a global warming perturbation. In (a), the black line indicates the climatological temperature and tapered arrows indicate convergent or divergent energy flows, emphasizing the difference between the surface inversion layer—where atmospheric cooling is mediated by energy transfer to the surface and subsequent radiative loss to space (the surface radiator fin)—and in the free atmosphere, where cooling occurs by direct atmospheric emission to space. In (b), the green line shows the imposed T_e^{in} anomaly (which is inherently bottom-heavy due to increased latent heat content near the surface), the black line shows the polar temperature response, and gray arrows indicate warming or cooling tendencies due to different mechanisms as in noted in the figure.

to a stronger inversion. Vice-versa, warming the surface through decreased albedo or blocking the water-vapor window by increased greenhouse gas concentration will weaken the inversion. As indicated in Figure 10b, these changes to the lower-tropospheric temperature structure are superposed on an overall increase in lapse rate throughout the column due to relaxation toward an equivalent temperature perturbation ΔT_e^{in} that is intrinsically bottom-heavy. Furthermore, increasing humidity results in increased upper-level radiative cooling, which tends to further increase the overall lapse rate.

2. *Why do changes in moist and dry energy transport to the poles tend to mutually compensate, and what constraints act to enforce this compensation?*

Given typical temperatures in Earth's modern climate, warming the low-level inflow to the polar caps causes comparable changes in dry and latent energy content of the inflowing air masses, while a similar perturbation to outflow temperature causes a much smaller change in latent energy content. This means that essentially all additional moisture entering the polar cap in a warmed climate will condense and release its latent heat—moist energy convergence can increase, but not decrease in response to warming. On the other hand, the strong reduction of radiator fin strength in response to warming (see point 1 above) requires an overall reduction in energy convergence at low levels, which can only be accomplished by a warming of the outflow and reduced dry energy convergence. Compensation between dry and moist energy transport is therefore a robust, thermodynamically-constrained response at low levels. At upper levels, both inflow and outflow temperatures are low enough that moisture plays a negligible role. Increased upper-level radiative cooling in response to warming is thus balanced by increased dry energy convergence. Overall, the precise degree of compensation between vertically-integrated moist and dry transport depends delicately on radiative responses at different levels and is not robust.

3. *What is the best way to decompose forcing and feedbacks at the poles?*

In agreement with previous work on RAE, our analysis suggests that lapse-rate feedback at the poles does not constitute a well-defined standalone mechanism: different forcing and feedback agents affect the lapse rate differently and through disparate mechanisms. More fundamentally, in RAE there is no strong relationship between surface temperature and TOA radiative fluxes, since much of the outgoing longwave radiation originates in the mid- to upper troposphere which is decoupled from the surface. It makes more sense therefore to think only in terms of a temperature response which includes a lapse-rate response whose structure is controlled by the mechanisms explore above.

We go a step further, and argue that remote influence—represented here by the inflow equivalent temperature profile T_e^{in}—should be considered an external forcing, since it affects polar climate but is not affected by it to a first approximation (i.e., remote influence is felt as a change in boundary conditions). Part of the temperature response to both local and remote forcing is an adjustment to bring changes in diabatic cooling into equilibrium with changes in advective heating. Just as in the case of the lapse-rate feedback, these adjustments are different for different forcing agents, so again it does not make sense to think of a single, standalone advective heating feedback, but rather of a temperature response which includes the advective heating adjustment.

In conclusion, we believe that the single-column model explored here—and the concepts and mechanisms elucidated by this exploration—provides a useful basic framework for thinking about the polar climate. It is certainly an incomplete framework as it stands. It lacks a description of cloud effects—in particular, high-opacity low-level clouds can be expected to substantially affect the functioning of the surface radiator fin and could strongly affect the surface temperature response (Cronin and Tziperman 2015; Dimitrelos et al. 2023), though much uncertainty still surrounds the overall impact of clouds on polar climate (Kay et al. 2016). Our model also assumes a homogeneous surface, lacking a description of partial sea-ice cover and an explicit surface-albedo feedback. Understanding whether these additional effects lead to qualitatively different behavior, or rather just a quantitative modification of the basic clear-sky picture developed here, provides an interesting avenue for future work. In addition, our work provides a novel feedback decomposition which can in principle be straightforwardly applied to analyse full climate model responses, using only readily-available temperature and humidity profiles as input. Further exploration of this possibility provides a further avenue for future work.

Acknowledgments. We thank Nadir Jeevanjee for useful comments.

Data availability statement. The CliMT modelling framework is available at https://github.com/CliMT/climt. The ERA-Interim reanalysis product may be obtained as detailed here: https://confluence.ecmwf.int/display/CKB/How+to+download+ERA-Interim+data+from+the+ECMWF+data+archive.

References

Andry, O., R. Bintanja, and W. Hazeleger, 2017: Time-dependent variations in the Arctic's surface albedo feedback and the link to seasonality in sea ice. *J. Climate*, **30**, 393–410.

Armour, K. C., N. Siler, A. Donohoe, and G. H. Roe, 2019: Meridional atmospheric heat transport constrained by energetics and mediated by large-scale diffusion. *J. Climate*, **32**, 3655–3680, https://doi.org/10.1175/JCLI-D-18-0563.1.

Audette, A., and Coauthors, 2021: Opposite responses of the dry and moist eddy heat transport into the Arctic in the PAMIP experiments. *Geophys. Res. Lett.*, **48**, e2020GL089 990.

Beer, E., and I. Eisenman, 2022: Revisiting the role of the water vapor and lapse rate feedbacks in the Arctic amplification of climate change. *J. Climate*, **35**, 2975–2988.

Caballero, R., R. Pierrehumbert, and J. Mitchell, 2008: Axisymmetric, nearly inviscid circulations in non-condensing radiative-convective atmospheres. *Quart. J. Roy. Meteor. Soc.*, **134**, 1269–1285.

Cardinale, C. J., B. E. Rose, A. L. Lang, and A. Donohoe, 2021: Stratospheric and tropospheric flux contributions to the polar cap energy budgets. *J. Climate*, **34**, 4261–4278.

Chang, C.-Y., and T. M. Merlis, 2022: The role of diffusivity changes on the pattern of warming in energy balance models. *J. Climate*, **36**, 7993–8006.

Chen, Y.-T., Y. Huang, and T. M. Merlis, 2023: The global patterns of instantaneous CO_2 forcing at the top-of-atmosphere and surface. *J. Climate*, **36**, 6331–6347.

Chen, Y.-T., T. M. Merlis, and Y. Huang, 2024: The cause of negative CO_2 forcing at the top-of-atmosphere: the role of stratospheric vs. tropospheric temperature inversions. *Geophys. Res. Lett.*, **51**, e2023GL106 433.

Chung, C. E., and P. Räisänen, 2011: Origin of the Arctic warming in climate models. *Geophys. Res. Lett.*, **38**, L21 704.

Collins, W. D., and Coauthors, 2004: Description of the NCAR community atmosphere model (CAM 3.0). *NCAR Tech. Note NCAR/TN-464+ STR*, **226**.

Colman, R., J. Fraser, and L. Rotstayn, 2001: Climate feedbacks in a general circulation model incorporating prognostic clouds. *Clim. Dyn.*, **18**, 103–122.

Cronin, T. W., and M. F. Jansen, 2016: Analytic radiative-advective equilibrium as a model for high-latitude climate. *Geophys. Res. Lett.*, **43**, 449–457.

Cronin, T. W., and E. Tziperman, 2015: Low clouds suppress Arctic air formation and amplify high-latitude continental winter warming. *Proc. Natl. Acad. Sci. USA*, **112**, 11 490–11 495.

Curry, J., 1983: On the formation of continental polar air. *J. Atmos. Sci.*, **40**, 2278–2292.

Dimitrelos, A., R. Caballero, and A. M. Ekman, 2023: Controls on surface warming by winter Arctic moist intrusions in idealized large-eddy simulations. *J. Climate*, **36**, 1287–1300.

Feldl, N., B. T. Anderson, and S. Bordoni, 2017: Atmospheric eddies mediate lapse rate feedback and Arctic amplification. *J. Climate*, **30**, 9213–9224.

Feldl, N., and T. M. Merlis, 2021: Polar amplification in idealized climates: the role of ice, moisture, and seasons. *Geophys. Res. Lett.*, e2021GL094130.

Feldl, N., S. Po-Chedley, H. K. A. Singh, S. Hay, and P. J. Kushner, 2020: Sea ice and atmospheric circulation shape the high-latitude lapse rate feedback. *npj Clim. Atmos. Sci.*, **3**, 1–9.

Freese, L. M., and T. W. Cronin, 2021: Antarctic radiative and temperature responses to a doubling of CO_2. *Geophys. Res. Lett.*, **48**, e2021GL093 676.

Hahn, L., K. C. Armour, D. S. Battisti, A. Donohoe, A. Pauling, and C. Bitz, 2020: Antarctic elevation drives hemispheric asymmetry in polar lapse-rate climatology and feedback. *Geophys. Res. Lett.*, **47**, e2020GL088 965.

Hahn, L. C., K. C. Armour, M. D. Zelinka, C. M. Bitz, and A. Donohoe, 2021: Contributions to polar amplification in CMIP5 and CMIP6 models. *Front. Earth Sci.*, **9**, 710 036.

Henry, M., T. Merlis, N. Lutsko, and B. E. Rose, 2021: Decomposing the drivers of polar amplification with a single column model. *J. Climate*, **34**, 2355–2365.

Henry, M., and T. M. Merlis, 2020: Forcing dependence of atmospheric lapse rate changes dominates residual polar warming in solar radiation management climate scenarios. *Geophys. Res. Lett.*, **47**, e2020GL087 929.

Hwang, Y.-T., D. M. Frierson, and J. E. Kay, 2011: Coupling between Arctic feedbacks and changes in poleward energy transport. *Geophys. Res. Lett.*, **38**, 17 704.

Jeevanjee, N., and S. Fueglistaler, 2020: Simple spectral models for atmospheric radiative cooling. *J. Atmos. Sci.*, **77**, 479–497.

Jeevanjee, N., I. Held, and V. Ramaswamy, 2022: Manabe's radiative–convective equilibrium. *Bull. Am. Meteorol. Soc.*, **103**, E2559–E2569.

Jeevanjee, N., J. T. Seeley, D. Paynter, and S. Fueglistaler, 2021: An analytical model for spatially varying clear-sky CO_2 forcing. *J. Climate*, **34**, 9463–9480.

Kay, J. E., T. L'Ecuyer, H. Chepfer, N. Loeb, A. Morrison, and G. Cesana, 2016: Recent advances in Arctic cloud and climate research. *Curr. Clim. Change Rep.*, **2**, 159–169.

Kim, D., S. M. Kang, T. M. Merlis, and Y. Shin, 2021: Atmospheric circulation sensitivity to changes in the vertical structure of polar warming. *Geophys. Res. Lett.*, **48**, e2021GL094 726.

Koll, D. D., N. Jeevanjee, and N. J. Lutsko, 2023: An analytic model for the clear-sky longwave feedback. *J. Atmos. Sci.*, doi:10.1175/JAS–D–22–0178.1.

Manabe, S., and R. F. Strickler, 1964: Thermal equilibrium of the atmosphere with a convective adjustment. *J. Atmos. Sci.*, **21**, 361–385.

Manabe, S., and R. T. Wetherald, 1967: Thermal Equilibrium of the Atmosphere with a Given Distribution of Relative Humidity. *J. Atmos. Sci.*, **24**, 241–259.

Manabe, S., and R. T. Wetherald, 1980: On the distribution of climate change resulting from an increase in the CO_2 content of the atmosphere. *J. Atmos. Sci.*, **37**, 99–118.

Merlis, T. M., and M. Henry, 2018: Simple estimates of polar amplification in moist diffusive energy balance models. *J. Climate*, **31**, 5811–5824.

Miyawaki, O., T. A. Shaw, and M. F. Jansen, 2022: Quantifying energy balance regimes in the modern climate, their link to lapse rate regimes, and their response to warming. *J. Climate*, **35**, 1045–1061.

Miyawaki, O., T. A. Shaw, and M. F. Jansen, 2023: The emergence of a new wintertime Arctic energy balance regime. *Environ. Res.: Climate*, **2**, 031 003.

Monteiro, J. M., and R. Caballero, 2016: The Climate Modelling Toolkit. *Proceedings of the 15th Python in Science Conference (SciPy 2016)*, 69 – 74, doi:10.25 080/Majora–629e541a–014.

Monteiro, J. M., J. McGibbon, and R. Caballero, 2018: sympl (v. 0.4. 0) and climt (v. 0.15. 3)–towards a flexible framework for building model hierarchies in Python. *Geosci. Model Dev.*, **11**, 3781–3794.

Overland, J. E., and P. Turet, 1994: Variability of the atmospheric energy flux across 70°N computed from the GFDL Data Set. *The Polar Oceans and Their Role in Shaping the Global Environment*, Geophys. Monogr., Vol. 85, American Geophysical Union, 313–325.

Papritz, L., S. Murto, M. Röthlisberger, R. Caballero, G. Messori, G. Svensson, and H. Wernli, 2023: The role of local and remote processes for wintertime surface energy budget extremes over Arctic sea ice. *J. Climate*, **36**, 7657–7674.

Park, K., S. M. Kang, D. Kim, M. F. Stuecker, and F.-F. Jin, 2018: Contrasting local and remote impacts of surface heating on polar warming and amplification. *J. Climate*, **31**, 3155–3166.

Pauluis, O., A. Czaja, and R. Korty, 2010: The global atmospheric circulation in moist isentropic coordinates. *J. Climate*, **23**, 3077–3093.

Payne, A. E., M. F. Jansen, and T. W. Cronin, 2015: Conceptual model analysis of the influence of temperature feedbacks on polar amplification. *Geophys. Res. Lett.*, **42**, 9561–9570.

Pierrehumbert, R. T., 1995: Thermostats, radiator fins and the local runaway greenhouse. *J. Atmos. Sci.*, **52**, 1784–1806.

Pithan, F., and T. Mauritsen, 2014: Arctic amplification dominated by temperature feedbacks in contemporary climate models. *Nat. Geosci.*, **7**, 181–184.

Pithan, F., and Coauthors, 2018: Role of air-mass transformations in exchange between the Arctic and mid-latitudes. *Nat. Geosci.*, doi:10.1038/s41 561–018–0234–1.

Previdi, M., K. L. Smith, and L. M. Polvani, 2021: Arctic amplification of climate change: a review of underlying mechanisms. *Environ. Res. Lett.*, **16**, 093 003.

Russotto, R. D., and M. Biasutti, 2020: Polar amplification as an inherent response of a circulating atmosphere: Results from the TRACMIP aquaplanets. *Geophys. Res. Lett.*, **47**, e2019GL086 771.

Salzmann, M., 2017: The polar amplification asymmetry: role of Antarctic surface height. *Earth Syst. Dynam.*, **8**, 323–336.

Screen, J. A., C. Deser, and I. Simmonds, 2012: Local and remote controls on observed arctic warming. *Geophysical Research Letters*, **39**, L10 709.

Seeley, J. T., and N. Jeevanjee, 2021: H_2O windows and CO_2 radiator fins: A clear-sky explanation for the peak in equilibrium climate sensitivity. *Geophys. Res. Lett.*, **48**, e2020GL089 609.

Semmler, T., F. Pithan, and T. Jung, 2020: Quantifying two-way influences between the Arctic and mid-latitudes through regionally increased CO2 concentrations in coupled climate simulations. *Clim. Dyn.*, **54**, 3307–3321.

Shaw, T. A., and Z. Tan, 2018: Testing latitudinally dependent explanations of the circulation response to increased CO_2 using aquaplanet models. *Geophys. Res. Lett.*, **45**, 9861–9869.

Sherwood, S. C., S. Bony, O. Boucher, C. Bretherton, P. M. Forster, J. M. Gregory, and B. Stevens, 2015: Adjustments in the forcing-feedback framework for understanding climate change. *Bull. Am. Meteorol. Soc.*, **96**, 217–228.

Sobel, A. H., and C. S. Bretherton, 2000: Modeling tropical precipitation in a single column. *J. Climate*, **13**, 4378–4392.

Soden, B. J., I. M. Held, R. Colman, K. M. Shell, J. T. Kiehl, and C. A. Shields, 2008: Quantifying climate feedbacks using radiative kernels. *J. Climate*, **21**, 3504–3520.

Stuecker, M. F., and Coauthors, 2018: Polar amplification dominated by local forcing and feedbacks. *Nat. Clim. Change*, **8**, 1076–1081.

Taylor, P. C., and Coauthors, 2022: Process drivers, inter-model spread, and the path forward: A review of amplified Arctic warming. *Front. Earth Sci.*, **9**, 758 361, https://doi.org/10.3389/feart.2021.758361.

Trenberth, K. E., 1991: Climate diagnostics from global analyses: Conservation of mass in ECMWF analyses. *J. Climate*, **4**, 707–722.

Wexler, H., 1936: Cooling in the lower atmosphere and the structure of polar continental air. *Mon. Wea. Rev*, **64**, 122–136.

Woods, C., and R. Caballero, 2016: The role of moist intrusions in winter Arctic warming and sea ice decline. *J. Climate*, **29**, 4473–4485.

Yoshimori, M., A. Abe-Ouchi, and A. Laîné, 2017: The role of atmospheric heat transport and regional feedbacks in the arctic warming at equilibrium. *Clim. Dyn.*, **49**, 3457–3472.